nature physics

Letter

https://doi.org/10.1038/s41567-022-01762-1

Search for quantum gravity using astrophysical neutrino flavour with IceCube

Received: 18 November 2021

Accepted: 17 August 2022

Published online: 24 October 2022

Check for updates

The IceCube Collaboration*

Along their long propagation from production to detection, neutrinos undergo flavour conversions that convert their types or flavours[1,2]. High-energy astrophysical neutrinos propagate unperturbed over a billion light years in vacuum[3] and are sensitive to small effects caused by new physics. Effects of quantum gravity[4] are expected to appear at the Planck energy scale. Such a high-energy universe would have existed only immediately after the Big Bang and is inaccessible by human technologies. On the other hand, quantum gravity effects may exist in our low-energy vacuum[5–8], but are suppressed by inverse powers of the Planck energy. Measuring the coupling of particles to such small effects is difficult via kinematic observables, but could be observable through flavour conversions. Here we report a search with the IceCube Neutrino Observatory, using astrophysical neutrino flavours[9,10] to search for new space–time structure. We did not find any evidence of anomalous flavour conversion in the IceCube astrophysical neutrino flavour data. We apply the most stringent limits of any known technologies, down to 10^{-42} GeV^{-2} with Bayes factor greater than 10 on the dimension-six operators that parameterize the space–time defects. We thus unambiguously reach the parameter space of quantum-gravity-motivated physics.

In the past, quantum gravity (QG) was investigated by means of astrophysical neutrino spectrum distortion[11] and time-of-flight[12–14] measurements. In this Letter we focus on astrophysical neutrino flavour information to search for QG effects via neutrino interferometry. Neutrino interferometry[15] has been applied in various terrestrial neutrino experiments, but no evidence of QG has been found[16]. The sensitivity of neutrino interferometry for astrophysical neutrinos exceeds any terrestrial experiments because of the higher energies and longer propagation distances of the neutrinos involved (Fig. 1 provides an illustration).

Neutrino interactions with low-energy manifestations of QG can be modelled using effective operators[15], such as

$$H \sim \frac{m^2}{2E} + \mathring{a}^{(3)} - E\,\mathring{c}^{(4)} + E^2\,\mathring{a}^{(5)} - E^3\,\mathring{c}^{(6)} \cdots . \qquad (1)$$

The first term in this Hamiltonian describes the neutrino mass term[17], where we assume normal mass ordering as both mass ordering assumptions provide comparable results. All other terms ($\mathring{a}^{(3)}, \mathring{c}^{(4)}, \mathring{a}^{(5)}, \mathring{c}^{(6)}, \ldots$) represent new interactions, such as those between neutrinos and space–time defects. In particular, QG effects are well-motivated in higher-dimensional operators ($\mathring{a}^{(5)}, \mathring{c}^{(6)}, \ldots$)[18], the presence of which is a sign of an undiscovered high-energy scale, such as the Planck scale. For example, the Fermi constant associated with a dimension-six operator was one of the first manifestations of electroweak theory. These terms correspond to the isotropic part of the Standard-Model Extension (SME)[19], which is an effective field theory that describes the effects of particle Lorentz violation. All terms are 3 × 3 complex matrices in the neutrino flavour basis. There are three neutrino flavours: electron-neutrino (ν_e), muon-neutrino (ν_μ) and tau-neutrino (ν_τ). The solution of this Hamiltonian describes the evolution of neutrino flavours. Because the astrophysical flux normalization is unknown,

*A list of authors and their affiliations appears at the end of the paper. e-mail: analysis@icecube.wisc.edu

https://doi.org/10.1038/s41567-022-01762-1

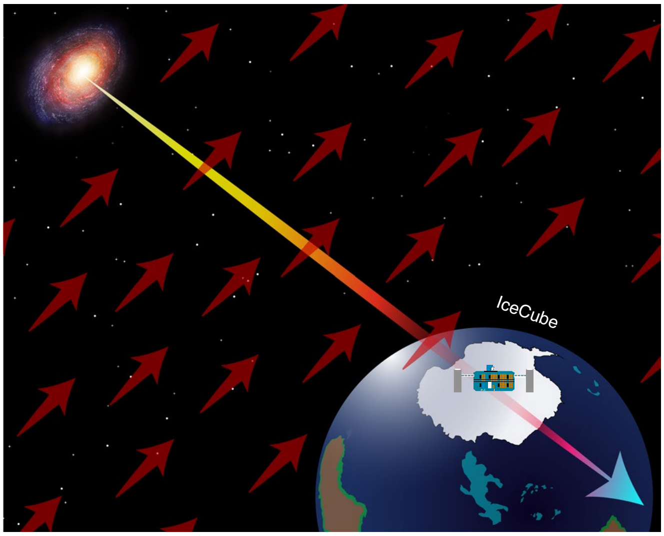

Fig. 1 | Illustration of this analysis. High-energy astrophysical neutrinos, from 60 TeV to 2 PeV, are emitted from distant high-energy sources, change flavour during propagation (shown by the long multicoloured arrow) and are detected by IceCube (not to scale). The neutrino propagation may be affected by space–time defects, which can be viewed as an æther-like medium in vacuum, and in general these defects have directions as depicted by red arrows. Although the effect may depend on direction, we assume it is isotropic in our frame, without loss of generality, as the data are compatible with an isotropic distribution[9].

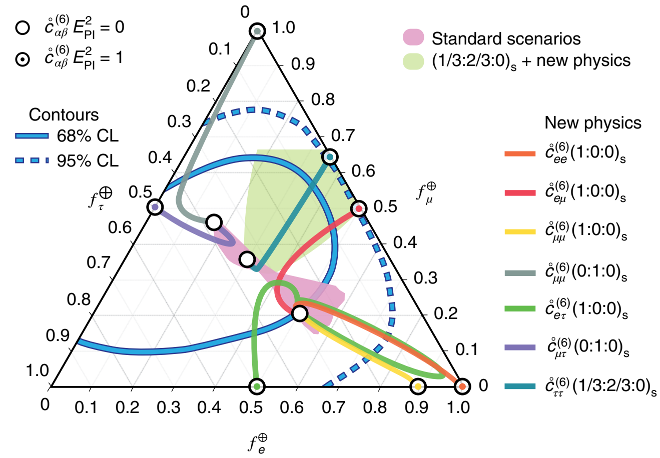

Fig. 2 | Astrophysical neutrino flavour triangle, including illustrations of new physics effects and data contours. The figure represents the flavour ratio expected on Earth ($f_e^\oplus : f_\mu^\oplus : f_\tau^\oplus$) for given compositions at the source (S). The corners indicate pure ν_e, ν_μ or ν_τ composition. The blue solid and dashed lines show the 68% and 95% CL contours[10] from IceCube data. The pink region represents expected flavour ratios from the standard astrophysical neutrino production models, where the neutrinos at the production source are all possible combinations of ν_e and ν_μ (the neutrino oscillation parameter errors are given in ref. [17]). The green region is the expected flavour ratio from the preferred scenario $(1/3{:}2/3{:}0)_S$ with any new physics scenario. The lines explained in the lower legend illustrate the effects of the $\mathring{c}^{(6)}_{\alpha\beta}$ new physics operators introduced in equation (1). Three astrophysical neutrino production models are highlighted by ○ symbols, a ν_μ-dominant source $(0{:}1{:}0)_S$ (top), a ν_e-dominant source $(1{:}0{:}0)_S$ (bottom) and a preferred model $(1/3{:}2/3{:}0)_S$ (middle). When new physics operators are small ($\lesssim m^2/2E$), they are distributed within the central region. If the values of new physics operators are increased, predicted flavour ratios start to move away from the centre, and they reach to the ⊙ symbols with large new physics such as $\mathring{c}^{(6)}_{\alpha\beta} = E_{\rm Pl}^{-2}$ where $E_{\rm Pl} = 1.22\times10^{19}$ GeV is the Planck energy. For simplicity we concentrate on real, positive new physics potentials.

neutrino flavour is measured in terms of the flavour ratio ($\nu_e{:}\nu_\mu{:}\nu_\tau$), which is a normalized fraction of each flavour defined after integrating expected astrophysical neutrino spectra. The measured flavour ratio depends on the production mechanisms of astrophysical neutrinos at their sources and on the effective Hamiltonian. Further details of the formulation are provided in the Methods.

The IceCube Neutrino Observatory[20] is an array of 5,160 digital optical modules (DOMs) embedded in the Antarctic ice between 1,450 m and 2,450 m below the surface. Each DOM contains one 25.4-cm photomultiplier tube in a glass shell, and it detects light from charged particles produced by neutrino interactions. A series of 60 DOMs are connected with a vertical spacing of 17 m to make one string, and 86 strings with ~125-m separation cover a 1-km^3 volume of natural ice as a target volume for astrophysical neutrinos.

When neutrinos undergo charged-current interactions, they generate charged leptons whose types depend on the neutrino flavours. In other words, an ν_e ($\bar{\nu}_e$) creates an electron (positron), a ν_μ ($\bar{\nu}_\mu$) creates a muon (anti-muon), and a ν_τ ($\bar{\nu}_\tau$) creates a tau (anti-tau). These charged leptons generate characteristic light emission distributions in IceCube. Electrons initiate electromagnetic showers in ice that look like an approximately isotropic emission of photons (cascade), muons emit light along their straight trajectories (track), and some taus produce an isotropic emission with a slight elongation, reflecting bursts of photon emission from the production of the tau and its subsequent decay (double cascade). However, most taus from charged-current interactions and hadronic showers from neutral-current interactions also lead to cascades. A likelihood function is constructed from the time and charge distributions of DOMs to estimate the energies, directions and flavours of the neutrinos. Charged leptons and charged anti-leptons have indistinguishable light emission profiles in ice.

In this analysis we use the High-Energy Starting Event (HESE) sample, which comprises 7.5 years of data collection from 2010 to 2018[9]. A total of 60 events above 60 TeV are observed. Among these, 41, 17 and 2 events are classified as cascades, tracks and double cascades, respectively. At most, ten of the lowest-energy events are expected to be atmospheric neutrino foreground. Cascades and tracks are distributed in ten incoming zenith angle bins, in the range $\cos\theta_z = [-1.0, +1.0]$, with $\cos\theta_z = +1.0$ pointing to the celestial south pole. We use 20 natural logarithmic bins in deposited energy in the range E = [60 TeV, 2 PeV]. For the double cascade events, there are ten bins in the reconstructed distance between two cascade signals L = [10 m, 100 m] instead of zenith angle bins. The median neutrino energy (zenith angle) resolutions for reconstructed cascades, tracks and double cascades are 11% (6.3°), 30% (1.5°) and 18% (5.0°), respectively.

The expected number of events in each bin is computed through a Monte Carlo (MC) simulation. First, the astrophysical neutrino flux is modelled as a single power-law spectrum. This is weighted with the assumed flavour ratio at the source and the mixing probability derived from the effective Hamiltonian including new physics operators (equation (1)). The foreground flux due to atmospheric neutrinos from π and K-decays[21], charm meson decays[22] and atmospheric muons[23] is added to simulate the complete flux arriving at the detector. Neutrino absorption in the Earth is modelled using a standard Earth density profile[24]. Particles produced by neutrino interactions[25] are computed using specialized MC[26] to output photon signals.

Figure 2 shows a comparison of the HESE 7.5-yr flavour ratio measurement[10] with model predictions. This flavour triangle diagram represents astrophysical neutrino flavour ratios, with each point in the diagram showing the energy-averaged flavour composition at Earth. The pink region near the centre denotes the so-called standard scenarios. This represents all possible flavour ratios at Earth from standard astrophysical neutrino production mechanisms via neutrino mixing[27]. As shown, all of the standard flavour ratios are enclosed in the 95% confidence level (CL) contour, which implies that, at this moment,

https://doi.org/10.1038/s41567-022-01762-1

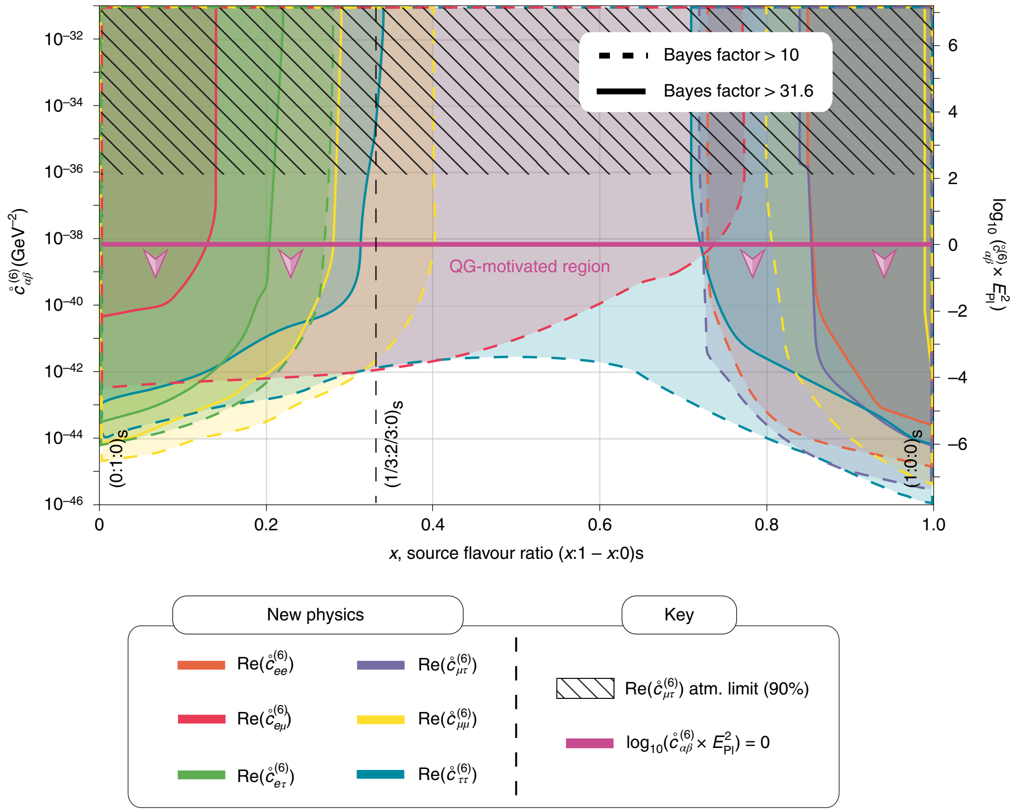

Fig. 3 | Limits on the dimension-six new physics operator. The QG-motivated region is defined by $\log_{10}(\mathring{c}^{(6)}_{\alpha\beta} \times E^2_{\rm Pl}) < 0$, and is indicated by a horizontal magenta line and arrowheads. The hatched region is the limit obtained from the atmospheric neutrino data analysis on Re ($\mathring{c}^{(6)}_{\mu\tau}$) (ref. [15]). Limits determined by Bayes factors >10 (dashed lines) and >31.6 (solid lines) are presented as a function of the assumed astrophysical neutrino flavour ratio at the production source. The leftmost scenario is ν_μ-dominant $(0{:}1{:}0)_{\rm S}$ and the rightmost is ν_e-dominant $(1{:}0{:}0)_{\rm S}$. The preferred scenario corresponds to $(1/3{:}2/3{:}0)_{\rm S}$ (dashed vertical line). Limits on Re ($\mathring{c}^{(6)}_{ee}$) (orange), Re ($\mathring{c}^{(6)}_{e\mu}$) (red), Re ($\mathring{c}^{(6)}_{e\tau}$) (green), Re ($\mathring{c}^{(6)}_{\mu\mu}$) (yellow), Re ($\mathring{c}^{(6)}_{\mu\tau}$) (purple) and Re ($\mathring{c}^{(6)}_{\tau\tau}$) (blue) are shown.

Table 1 | Limits on new physics operators extracted from this analysis

Dim	Coefficient	Limit (BF>10)
3	Re ($\mathring{a}^{(3)}_{\tau\tau}$)	2×10^{-26} GeV
4	Re ($\mathring{c}^{(4)}_{\tau\tau}$)	2×10^{-31}
5	Re ($\mathring{a}^{(5)}_{\tau\tau}$)	2×10^{-37} GeV^{-1}
6	Re ($\mathring{c}^{(6)}_{\tau\tau}$)	3×10^{-42} GeV^{-2}
7	Re ($\mathring{a}^{(7)}_{\tau\tau}$)	3×10^{-47} GeV^{-3}
8	Re ($\mathring{c}^{(8)}_{\tau\tau}$)	2×10^{-52} GeV^{-4}

These limits on new physics operators are derived from BF>10, which corresponds to a 1 in 10 likelihood ratio for a uniform prior. Limits that depend on assumed production source models are listed in Extended Data Table 1.

all models within standard scenarios are allowed. In other words, the IceCube HESE flavour measurement is consistent with the standard scenarios, given current statistics and systematic errors. However, current data exclude certain QG models that produce flavour compositions far away from the standard region, because any new structure in the vacuum would produce detectable anomalous flavour ratios, shown by lines in Fig. 2.

To make a quantitative statement about these scenarios, we performed a likelihood analysis and report the results using a Bayesian method. Our analysis includes all of the flux components previously discussed in the text and implements their systematics according to the prescription given in ref. [9]. Our analysis likelihood includes nuisance parameters to incorporate the flux and detector uncertainties, standard oscillation parameters and neutrino mass differences, and parameters that incorporate the QG effective operators. Technical details of the fit methods and the systematic errors are provided in the Methods and Extended Data Figs. 1 and 2.

Figure 3 presents the results for the dimension-six operators. The results for other operators are summarized in Extended Data Figs. 3–7. These represent new physics interactions and we expect the QG-motivated physics operator to be of order $E_{\rm Pl}^{-2} = 6.7 \times 10^{-39}$ GeV^{-2}, where $E_{\rm Pl} = 1.22 \times 10^{19}$ GeV is the Planck energy. Limits are shown on a log scale. The right axis incorporates an additional $E^2_{\rm Pl}$ factor where below zero corresponds to the QG-motivated physics signal region. We reach the QG-motivated signal region of the dimension-six operator with neutrinos. The limits are a function of the astrophysical neutrino production model at the source.

Strong limits are obtained for ν_μ-dominant $(0{:}1{:}0)_{\rm S}$ and ν_e-dominant $(1{:}0{:}0)_{\rm S}$ scenarios. The ν_μ-dominant scenarios are expected in accelerators such as active galactic nuclei, and ν_e-dominant scenarios are expected in accelerators such as neutron stars[28]. Substantial limits for Re ($\mathring{c}^{(6)}_{\tau\tau}$) are obtained across all astrophysical neutrino models including the preferred scenario $(1/3{:}2/3{:}0)_{\rm S}$, which is based on astrophysical pion and muon decays. Muon energy loss in the source can cause the ν_e fraction to be lower than 1/3, where our limits are valid. The shapes of the limit curves in Fig. 3 are understood from Fig. 2. Here, non-zero Re ($\mathring{c}^{(6)}_{e\tau}$) with $(1{:}0{:}0)_{\rm S}$ and Re ($\mathring{c}^{(6)}_{\mu\tau}$) with $(0{:}1{:}0)_{\rm S}$ models are enclosed by the contour. This suggests that the data cannot set limits on these scenarios. On the other hand, the data reject certain scenarios, such as a non-zero Re $(\mathring{c}_{ee}^{(6)})$ model or a Re $(\mathring{c}_{\mu\mu}^{(6)})$ model with $(1:0:0)_S$. For the preferred scenario, $(1/3:2/3:0)_S$, any new physics scenario is described by the green region, and is almost enclosed by the 95% CL contour. Given this, only a few substantial limits can be achieved, for example, Re $(\mathring{c}_{e\mu}^{(6)})$ and Re $(\mathring{c}_{\tau\tau}^{(6)})$.

In Table 1, scenario-independent limits obtained from Bayes factors (BFs) > 10 are quoted. These are defined by taking into account a full range of allowed standard astrophysical neutrino production models. Although the motivation of this analysis is to look for evidence of QG, the formalism we have used is model-independent, and our results can set limits on various new physics models[29], including a new long-range force[30], neutrino–dark energy coupling[31], neutrino–dark matter scattering[32], violation of equivalent principle[33] and so on.

Online content

Any methods, additional references, Nature Research reporting summaries, source data, extended data, supplementary information, acknowledgements, peer review information; details of author contributions and competing interests; and statements of data and code availability are available at https://doi.org/10.1038/s41567-022-01762-1.

References

1. Fukuda, Y. et al. Evidence for oscillation of atmospheric neutrinos. *Phys. Rev. Lett.* **81**, 1562–1567 (1998).
2. Ahmad, Q. R. et al. Measurement of the rate of $\nu_e + d \rightarrow p + p + e^-$ interactions produced by ^{8}B solar neutrinos at the Sudbury Neutrino Observatory. *Phys. Rev. Lett.* **87**, 071301 (2001).
3. Aartsen, M. G. et al. Neutrino emission from the direction of the blazar TXS 0506+056 prior to the IceCube-170922A alert. *Science* **361**, 147–151 (2018).
4. Hawking, S. W. The unpredictability of quantum gravity. *Commun. Math. Phys.* **87**, 395–415 (1982).
5. Kostelecky, V. A. & Samuel, S. Spontaneous breaking of Lorentz symmetry in string theory. *Phys. Rev. D* **39**, 683–685 (1989).
6. Amelino-Camelia, G., Ellis, J. R., Mavromatos, N. E., Nanopoulos, D. V. & Sarkar, S. Tests of quantum gravity from observations of gamma-ray bursts. *Nature* **393**, 763–765 (1998).
7. Pospelov, M. & Shang, Y. On Lorentz violation in Horava-Lifshitz type theories. *Phys. Rev. D* **85**, 105001 (2012).
8. Addazi, A. Quantum gravity phenomenology at the dawn of the multi-messenger era—a review. *Prog. Part. Nucl. Phys.* **125**, 103948 (2022).
9. Abbasi, R. et al. The IceCube high-energy starting event sample: description and flux characterization with 7.5 years of data. *Phys. Rev. D* **104**, 022002 (2021).
10. Abbasi, R. et al. [IceCube] Measurement of astrophysical tau neutrinos in IceCube's high-energy starting events. Preprint at https://arxiv.org/abs/2011.03561 (2020).
11. Diaz, J. S., Kostelecky, A. & Mewes, M. Testing relativity with high-energy astrophysical neutrinos. *Phys. Rev. D* **89**, 043005 (2014).
12. Ellis, J., Mavromatos, N. E., Sakharov, A. S. & Sarkisyan-Grinbaum, E. K. Limits on neutrino Lorentz violation from multimessenger observations of TXS 0506+056. *Phys. Lett. B* **789**, 352–355 (2019).
13. Amelino-Camelia, G., D'Amico, G., Rosati, G. & Loret, N. In-vacuo-dispersion features for GRB neutrinos and photons. *Nat. Astron.* **1**, 0139 (2017).
14. Huang, Y. & Ma, B. Q. Lorentz violation from gamma-ray burst neutrinos. *Commun. Phys.* **1**, 62 (2018).
15. Aartsen, M. G. et al. Neutrino interferometry for high-precision tests of Lorentz symmetry with IceCube. *Nat. Phys.* **14**, 961–966 (2018).
16. Kostelecky, V. A. & Russell, N. Data tables for Lorentz and CPT violation. Preprint at https://arxiv.org/abs/0801.0287v15 (2022).
17. Esteban, I., Gonzalez-Garcia, M. C., Maltoni, M., Schwetz, T. & Zhou, A. The fate of hints: updated global analysis of three-flavor neutrino oscillations. *JHEP* **09**, 178 (2020).
18. Chalmers, M. Interview: Steven Weinberg. *CERN Courier* **57**(9), 31–35 (November 2017).
19. Kostelecky, A. & Mewes, M. Neutrinos with Lorentz-violating operators of arbitrary dimension. *Phys. Rev. D* **85**, 096005 (2012).
20. Aartsen, M. G. et al. The IceCube Neutrino Observatory: instrumentation and online systems. *J. Instrum.* **12**, P03012 (2017).
21. Honda, M., Kajita, T., Kasahara, K., Midorikawa, S. & Sanuki, T. Calculation of atmospheric neutrino flux using the interaction model calibrated with atmospheric muon data. *Phys. Rev. D* **75**, 043006 (2007).
22. Bhattacharya, A., Enberg, R., Reno, M. H., Sarcevic, I. & Stasto, A. Perturbative charm production and the prompt atmospheric neutrino flux in light of RHIC and LHC. *JHEP* **06**, 110 (2015).
23. Heck, D., Knapp, J., Capdevielle, J. N., Schatz, G. & Thouw, T. CORSIKA: a Monte Carlo code to simulate extensive air showers. Report number FZKA-6019 (1998); https://publikationen.bibliothek.kit.edu/270043064
24. Dziewonski, A. M. & Anderson, D. L. Preliminary reference earth model. *Phys. Earth Planet. Interiors* **25**, 297–356 (1981).
25. Cooper-Sarkar, A., Mertsch, P. & Sarkar, S. The high energy neutrino cross-section in the Standard Model and its uncertainty. *JHEP* **08**, 042 (2011).
26. Abbasi, R. et al. LeptonInjector and LeptonWeighter: a neutrino event generator and weighter for neutrino observatories. *Comput. Phys. Commun.* **266**, 108018 (2021).
27. Song, N., Li, S. W., Argüelles, C. A., Bustamante, M. & Vincent, A. C. The future of high-energy astrophysical neutrino flavor measurements. *J. Cosmol. Astropart. Phys.* **04**, 054 (2021).
28. Hümmer, S., Maltoni, M., Winter, W. & Yaguna, C. Energy dependent neutrino flavor ratios from cosmic accelerators on the Hillas plot. *Astropart. Phys.* **34**, 205–224 (2010).
29. Rasmussen, R. W., Lechner, L., Ackermann, M., Kowalski, M. & Winter, W. Astrophysical neutrinos flavored with Beyond the Standard Model physics. *Phys. Rev. D* **96**, 083018 (2017).
30. Bustamante, M. & Agarwalla, S. K. Universe's worth of electrons to probe long-range interactions of high-energy astrophysical neutrinos. *Phys. Rev. Lett.* **122**, 061103 (2019).
31. Klop, N. & Ando, S. Effects of a neutrino-dark energy coupling on oscillations of high-energy neutrinos. *Phys. Rev. D* **97**, 063006 (2018).
32. Farzan, Y. & Palomares-Ruiz, S. Flavor of cosmic neutrinos preserved by ultralight dark matter. *Phys. Rev. D* **99**, 051702 (2019).
33. Fiorillo, D. F. G., Mangano, G., Morisi, S. & Pisanti, O. IceCube constraints on violation of equivalence principle. *J. Cosmol. Astropart. Phys.* **04**, 079 (2021).

The IceCube Collaboration✉

R. Abbasi[1], M. Ackermann[2], J. Adams[3], J. A. Aguilar[4], M. Ahlers[5], M. Ahrens[6], J. M. Alameddine[7], C. Alispach[8], A. A. Alves Jr[9], N. M. Amin[10], K. Andeen[11], T. Anderson[12], G. Anton[13], C. Argüelles[14], Y. Ashida[15], S. Axani[16], X. Bai[17], A. Balagopal V[15], A. Barbano[8], S. W. Barwick[18], B. Bastian[2], V. Basu[15], S. Baur[4], R. Bay[19], J. J. Beatty[20,21], K.-H. Becker[22], J. Becker Tjus[23], C. Bellenghi[24], S. BenZvi[25], D. Berley[26], E. Bernardini[2,27], D. Z. Besson[28], G. Binder[19,29], D. Bindig[22], E. Blaufuss[26], S. Blot[2], M. Boddenberg[30], F. Bontempo[9], J. Borowka[30], S. Böser[31], O. Botner[32], J. Böttcher[30], E. Bourbeau[5], F. Bradascio[2], J. Braun[15], B. Brinson[33], S. Bron[8], J. Brostean-Kaiser[2], S. Browne[34], A. Burgman[32], R. T. Burley[35], R. S. Busse[36], M. A. Campana[37], E. G. Carnie-Bronca[35], C. Chen[33], Z. Chen[38], D. Chirkin[15], K. Choi[39], B. A. Clark[40], K. Clark[41], L. Classen[36], A. Coleman[10], G. H. Collin[16], J. M. Conrad[16], P. Coppin[42], P. Correa[42], D. F. Cowen[12,43], R. Cross[25], C. Dappen[30], P. Dave[33], C. De Clercq[42], J. J. DeLaunay[44], D. Delgado López[14], H. Dembinski[10], K. Deoskar[6], A. Desai[15], P. Desiati[15], K. D. de Vries[42], G. de Wasseige[45], M. de With[46], T. DeYoung[40], A. Diaz[16], J. C. Díaz-Vélez[15], M. Dittmer[36], H. Dujmovic[9], M. Dunkman[12], M. A. DuVernois[15], E. Dvorak[17], T. Ehrhardt[31], P. Eller[24], R. Engel[9,34], H. Erpenbeck[30], J. Evans[26], P. A. Evenson[10], K. L. Fan[26], K. Farrag[47], A. R. Fazely[48], N. Feigl[46], S. Fiedlschuster[13], A. T. Fienberg[12], K. Filimonov[19], C. Finley[6], L. Fischer[2], D. Fox[43], A. Franckowiak[2,23], E. Friedman[26], A. Fritz[31], P. Fürst[30], T. K. Gaisser[10], J. Gallagher[49], E. Ganster[30], A. Garcia[14], S. Garrappa[2], L. Gerhardt[29], A. Ghadimi[44], C. Glaser[32], T. Glauch[24], T. Glüsenkamp[13], J. G. Gonzalez[10], S. Goswami[44], D. Grant[40], T. Grégoire[12], S. Griswold[25], C. Günther[30], P. Gutjahr[7], C. Haack[24], A. Hallgren[32], R. Halliday[40], L. Halve[30], F. Halzen[15], M. Ha Minh[24], K. Hanson[15], J. Hardin[15], A. A. Harnisch[40], A. Haungs[9], D. Hebecker[46], K. Helbing[22], F. Henningsen[24], E. C. Hettinger[40], S. Hickford[22], J. Hignight[50], C. Hill[51], G. C. Hill[35], K. D. Hoffman[26], R. Hoffmann[22], B. Hokanson-Fasig[15], K. Hoshina[15,52], F. Huang[12], M. Huber[24], T. Huber[9], K. Hultqvist[6], M. Hünnefeld[7], R. Hussain[15], K. Hymon[7], S. In[39], N. Iovine[4], A. Ishihara[51], M. Jansson[6], G. S. Japaridze[53], M. Jeong[39], M. Jin[14], B. J. P. Jones[54], D. Kang[9], W. Kang[39], X. Kang[37], A. Kappes[36], D. Kappesser[31], L. Kardum[7], T. Karg[2], M. Karl[24], A. Karle[15], T. Katori[55], U. Katz[13], M. Kauer[15], M. Kellermann[30], J. L. Kelley[15], A. Kheirandish[12], K. Kin[51], T. Kintscher[2], J. Kiryluk[38], S. R. Klein[19,29], R. Koirala[10], H. Kolanoski[46], T. Kontrimas[24], L. Köpke[31], C. Kopper[40], S. Kopper[44], D. J. Koskinen[5], P. Koundal[9], M. Kovacevich[37], M. Kowalski[2,46], T. Kozynets[5], E. Kun[23], N. Kurahashi[37], N. Lad[2], C. Lagunas Gualda[2], J. L. Lanfranchi[12], M. J. Larson[26], F. Lauber[22], J. P. Lazar[14,15], J. W. Lee[39], K. Leonard[15], A. Leszczyńska[34], Y. Li[12], M. Lincetto[23], Q. R. Liu[15], M. Liubarska[50], E. Lohfink[31], C. J. Lozano Mariscal[36], L. Lu[15], F. Lucarelli[8], A. Ludwig[40,56], W. Luszczak[15], Y. Lyu[19,29], W. Y. Ma[2], J. Madsen[15], K. B. M. Mahn[40], Y. Makino[15], S. Mancina[15], S. Mandalia[47], I. C. Mariş[4], I. Martinez-Soler[14], R. Maruyama[57], K. Mase[51], T. McElroy[50], F. McNally[58], J. V. Mead[5], K. Meagher[15], S. Mechbal[2], A. Medina[21], M. Meier[51], S. Meighen-Berger[24], J. Micallef[40], D. Mockler[4], T. Montaruli[8], R. W. Moore[50], R. Morse[15], M. Moulai[16], R. Naab[2], R. Nagai[51], U. Naumann[22], J. Necker[2], L. V. Nguyên[40], H. Niederhausen[24], M. U. Nisa[40], S. C. Nowicki[40], A. Obertacke Pollmann[22], M. Oehler[9], B. Oeyen[59], A. Olivas[26], E. O'Sullivan[32], H. Pandya[10], D. V. Pankova[12], N. Park[41], G. K. Parker[54], E. N. Paudel[10], L. Paul[11], C. Pérez de los Heros[32], L. Peters[30], J. Peterson[15], S. Philippen[30], S. Pieper[22], M. Pittermann[34], A. Pizzuto[15], M. Plum[11], Y. Popovych[31], A. Porcelli[59], M. Prado Rodriguez[15], P. B. Price[19], B. Pries[40], G. T. Przybylski[29], C. Raab[4], A. Raissi[3], M. Rameez[5], K. Rawlins[60], I. C. Rea[24], A. Rehman[10], P. Reichherzer[23], R. Reimann[30], G. Renzi[4], E. Resconi[24], S. Reusch[2], W. Rhode[7], M. Richman[37], B. Riedel[15], E. J. Roberts[35], S. Robertson[19,29], G. Roellinghoff[39], M. Rongen[31], C. Rott[39,61], T. Ruhe[7], D. Ryckbosch[59], D. Rysewyk Cantu[40], I. Safa[14,15], J. Saffer[34], S. E. Sanchez Herrera[40], A. Sandrock[7], J. Sandroos[31], M. Santander[44], S. Sarkar[62], S. Sarkar[50], K. Satalecka[2], M. Schaufel[30], H. Schieler[9], S. Schindler[13], T. Schmidt[26], A. Schneider[15], J. Schneider[13], F. G. Schröder[9,10], L. Schumacher[24], G. Schwefer[30], S. Sclafani[37], D. Seckel[10], S. Seunarine[63], A. Sharma[32], S. Shefali[34], M. Silva[15], B. Skrzypek[14], B. Smithers[54], R. Snihur[15], J. Soedingrekso[7], D. Soldin[10], C. Spannfellner[24], G. M. Spiczak[63], C. Spiering[2], J. Stachurska[2], M. Stamatikos[21], T. Stanev[10], R. Stein[2], J. Stettner[30], A. Steuer[31], T. Stezelberger[29], T. Stürwald[22], T. Stuttard[5], G. W. Sullivan[26], I. Taboada[33], S. Ter-Antonyan[48], S. Tilav[10], F. Tischbein[30], K. Tollefson[40], C. Tönnis[64], S. Toscano[4], D. Tosi[15], A. Trettin[2], M. Tselengidou[13], C. F. Tung[33], A. Turcati[24], R. Turcotte[9], C. F. Turley[12], J. P. Twagirayezu[40], B. Ty[15], M. A. Unland Elorrieta[36], N. Valtonen-Mattila[32], J. Vandenbroucke[15], N. van Eijndhoven[42], D. Vannerom[16], J. van Santen[2], S. Verpoest[59], C. Walck[6], T. B. Watson[54], C. Weaver[40], P. Weigel[16], A. Weindl[9], M. J. Weiss[12], J. Weldert[31], C. Wendt[15], J. Werthebach[7], M. Weyrauch[34], N. Whitehorn[40,56], C. H. Wiebusch[30], D. R. Williams[44], M. Wolf[24], K. Woschnagg[19], G. Wrede[13], J. Wulff[23], X. W. Xu[48], J. P. Yanez[50], S. Yoshida[51], S. Yu[40], T. Yuan[15], Z. Zhang[38] and P. Zhelnin[14]

[1]Department of Physics, Loyola University Chicago, Chicago, IL, USA. [2]DESY, Zeuthen, Germany. [3]Department of Physics and Astronomy, University of Canterbury, Christchurch, New Zealand. [4]Université Libre de Bruxelles, Science Faculty CP230, Brussels, Belgium. [5]Niels Bohr Institute, University of Copenhagen, Copenhagen, Denmark. [6]Oskar Klein Centre and Department of Physics, Stockholm University, Stockholm, Sweden. [7]Department of Physics, TU Dortmund University, Dortmund, Germany. [8]Département de physique nucléaire et corpusculaire, Université de Genève, Genève, Switzerland. [9]Karlsruhe Institute of Technology, Institute for Astroparticle Physics, Karlsruhe, Germany. [10]Bartol Research Institute and Department of Physics and Astronomy, University of Delaware, Newark, DE, USA. [11]Department of Physics, Marquette University, Milwaukee, WI, USA. [12]Department of Physics, Pennsylvania State University, University Park, PA, USA. [13]Erlangen Centre for Astroparticle Physics, Friedrich-Alexander-Universität Erlangen-Nürnberg, Erlangen, Germany. [14]Department of Physics and Laboratory for Particle Physics and Cosmology, Harvard University, Cambridge, MA, USA. [15]Department of Physics and Wisconsin IceCube Particle Astrophysics Center, University of Wisconsin–Madison, Madison, WI, USA. [16]Department of Physics, Massachusetts Institute of Technology, Cambridge, MA, USA. [17]Physics Department, South Dakota School of Mines and Technology, Rapid City, SD, USA. [18]Department of Physics and Astronomy, University of California, Irvine, CA, USA. [19]Department of Physics, University of California, Berkeley, CA, USA. [20]Department of Astronomy, Ohio State University, Columbus, OH, USA. [21]Department of Physics and Center for Cosmology and Astro-Particle Physics, Ohio State University, Columbus, OH, USA. [22]Department of Physics, University of Wuppertal, Wuppertal, Germany. [23]Fakultät für Physik & Astronomie, Ruhr-Universität Bochum, Bochum, Germany. [24]Physik-department, Technische Universität München, Garching, Germany. [25]Department of Physics and Astronomy, University of Rochester, Rochester, NY, USA. [26]Department of Physics, University of Maryland, College Park, MD, USA. [27]Università di Padova, Padova, Italy. [28]Department of Physics and Astronomy, University of Kansas, Lawrence, KS, USA. [29]Lawrence Berkeley National Laboratory, Berkeley, CA, USA. [30]III. Physikalisches Institut, RWTH Aachen University, Aachen, Germany. [31]Institute of Physics, University of Mainz, Mainz, Germany. [32]Department of Physics and Astronomy, Uppsala University, Uppsala, Sweden. [33]School of Physics and Center for Relativistic Astrophysics, Georgia Institute of Technology, Atlanta, GA, USA. [34]Karlsruhe Institute of Technology, Institute of Experimental Particle Physics, Karlsruhe, Germany. [35]Department of Physics, University of Adelaide,

Adelaide, Australia. [36]Institut für Kernphysik, Westfälische Wilhelms-Universität Münster, Münster, Germany. [37]Department of Physics, Drexel University, Philadelphia, PA, USA. [38]Department of Physics and Astronomy, Stony Brook University, Stony Brook, NY, USA. [39]Department of Physics, Sungkyunkwan University, Suwon, Korea. [40]Department of Physics and Astronomy, Michigan State University, East Lansing, MI, USA. [41]Department of Physics, Engineering Physics, and Astronomy, Queen's University, Kingston, ON, Canada. [42]Vrije Universiteit Brussel (VUB), Dienst ELEM, Brussels, Belgium. [43]Department of Astronomy and Astrophysics, Pennsylvania State University, University Park, PA, USA. [44]Department of Physics and Astronomy, University of Alabama, Tuscaloosa, AL, USA. [45]Centre for Cosmology, Particle Physics and Phenomenology – CP3, Université Catholique de Louvain, Louvain-la-Neuve, Belgium. [46]Institut für Physik, Humboldt-Universität zu Berlin, Berlin, Germany. [47]Department of Physics and Astronomy, Queen Mary University of London, London, UK. [48]Department of Physics, Southern University, Baton Rouge, LA, USA. [49]Department of Astronomy, University of Wisconsin–Madison, Madison, WI, USA. [50]Department of Physics, University of Alberta, Edmonton, Alberta, Canada. [51]Department of Physics and Institute for Global Prominent Research, Chiba University, Chiba, Japan. [52]Earthquake Research Institute, University of Tokyo, Bunkyo, Tokyo, Japan. [53]CTSPS, Clark-Atlanta University, Atlanta, GA, USA. [54]Department of Physics, University of Texas at Arlington, Arlington, TX, USA. [55]Department of Physics, King's College London, London, UK. [56]Department of Physics and Astronomy, UCLA, Los Angeles, CA, USA. [57]Department of Physics, Yale University, New Haven, CT, USA. [58]Department of Physics, Mercer University, Macon, GA, USA. [59]Department of Physics and Astronomy, University of Gent, Gent, Belgium. [60]Department of Physics and Astronomy, University of Alaska Anchorage, Anchorage, AK, USA. [61]Department of Physics and Astronomy, University of Utah, Salt Lake City, UT, USA. [62]Department of Physics, University of Oxford, Oxford, UK. [63]Department of Physics, University of Wisconsin, River Falls, WI, USA. [64]Institute of Basic Science, Sungkyunkwan University, Suwon, Korea. ✉e-mail: analysis@icecube.wisc.edu

Methods

The notation of effective operators follows ref. [15]. Explicitly, equation (1) can be written as

$$H \sim \frac{m^2}{2E} + \begin{pmatrix} \mathring{a}^{(3)}_{ee} & \mathring{a}^{(3)}_{e\mu} & \mathring{a}^{(3)}_{\tau e} \\ \mathring{a}^{(3)*}_{e\mu} & \mathring{a}^{(3)}_{\mu\mu} & \mathring{a}^{(3)}_{\mu\tau} \\ \mathring{a}^{(3)*}_{\tau e} & \mathring{a}^{(3)*}_{\mu\tau} & \mathring{a}^{(3)}_{\tau\tau} \end{pmatrix} - E \begin{pmatrix} \mathring{c}^{(4)}_{ee} & \mathring{c}^{(4)}_{e\mu} & \mathring{c}^{(4)}_{\tau e} \\ \mathring{c}^{(4)*}_{e\mu} & \mathring{c}^{(4)}_{\mu\mu} & \mathring{c}^{(4)}_{\mu\tau} \\ \mathring{c}^{(4)*}_{\tau e} & \mathring{c}^{(4)*}_{\mu\tau} & \mathring{c}^{(4)}_{\tau\tau} \end{pmatrix} + \cdots . \quad (2)$$

Beyond the standard terms, there are two groups of new coefficients: the *CPT*-odd terms ($\mathring{a}^{(3)}$, $\mathring{a}^{(5)}$, $\mathring{a}^{(7)}$, ...) and the *CPT*-even terms ($\mathring{c}^{(4)}$, $\mathring{c}^{(6)}$, $\mathring{c}^{(8)}$, ...). The signs follow the convention of the SME given in ref. [19]. The integers in parentheses represent the dimension d of each operator. Hence, the units of these operators are GeV^{4-d}. The dimension-three and dimension-four operators are renormalizable, but all other operators are non-renormalizable. All effective operators affecting neutrino flavour conversions have Lorentz indices with temporal, spatial and mixed components in the Sun-centred celestial equatorial frame (SCCEF)[16]. However, the astrophysical neutrino flux assumed in this analysis is the diffuse flux. Hence, we assume that the incoming neutrino directions are uniform. This averages out any spatial effects, so this analysis is only sensitive to the isotropic flux component. This is reflected in our notation by the circles on top of the operators, indicating these operators are spatially isotropic.

In general, two or more operators with different dimensions (such as $\mathring{a}^{(3)}_{ee}$ and $\mathring{c}^{(4)}_{ee}$) may simultaneously affect the astrophysical neutrino flavour ratio. However, this is only relevant if the operator scales happen to have similar relative size in the energy region of this analysis. We hypothesize that this is an unlikely coincidence and here we do not assume this possibility. To simplify this analysis, we take only one of the operators to be non-vanishing when reporting our results. It is also possible to assume two elements from the same dimensional operator (such as $\mathring{a}^{(3)}_{ee}$ and $\mathring{a}^{(3)}_{e\mu}$). Because all elements are complex numbers, limits can be set for both real and imaginary parts (such as $\mathrm{Re}\,(\mathring{a}^{(3)}_{ee})$ and $\mathrm{Im}\,(\mathring{a}^{(3)}_{ee})$). However, the available data statistics does not allow us to fit two operators with identical energy dimension simultaneously. Such assumptions were relaxed in ref. [15]. The data sample is a mixture of neutrinos and antineutrinos, and we cannot distinguish them on an event-by-event basis. To assess the impact of the ratio of neutrinos to antineutrinos, we tested the impact of neutrino-only and antineutrino-only fits with a toy MC. The result of this test yields only marginal changes to the results. It was found that the complex phase had a small effect on the limits. Hence, for this analysis we search for one non-negative real element of each operator at a time.

The solution of the effective Hamiltonian (equation (1)) is used to compute the flavour ratio. We follow the procedure outlined in ref. [34]. First, neutrino flavour eigenstates $|\nu_\alpha\rangle$ can be described by the superposition of Hamiltonian eigenstates $|\nu_i\rangle$:

$$|\nu_\alpha\rangle = \sum_i V_{\alpha i}(E)|\nu_i\rangle. \quad (3)$$

Here, $V_{\alpha i}(E)$ is a unitary transformation that diagonalizes the effective Hamiltonian (equation (1)) to describe the mixing of neutrinos. Given the large baseline traversed and the energies involved, the resulting neutrino oscillation frequencies are very large and are averaged out by the detector energy resolution. In this regime, the transition probability of neutrinos can be written only through mixing matrix elements, which are the solution of the effective Hamiltonian. Explicitly, we find

$$P_{\nu_\alpha \to \nu_\beta}(E) = \sum_i |V_{\alpha i}(E)|^2 |V_{\beta i}(E)|^2. \quad (4)$$

The introduction of new interactions in vacuum through the new physics operators $\mathring{a}^{(3)}$, $c^{\circ(4)}$, $\mathring{a}^{(5)}$, $c^{\circ(6)}$, ... is imprinted in the mixing matrix element, $V_{\alpha i}(E)$, which can be determined through the neutrino mixing. The observable of interest is the neutrino flux of flavour β at Earth, $\phi^{\oplus}_{\beta}(E)$, and not the neutrino mixing itself. Note that the flux composition at Earth also depends on the initial neutrino flux of flavour α at the source, $\phi^{i}_{\alpha}(E)$. Furthermore, the small sample of astrophysical neutrinos restricts us to the use of the energy-averaged flavour composition:

$$\bar{\phi}^{\oplus}_{\beta} = \frac{1}{|\Delta E|} \int_{\Delta E} \sum_\alpha \bar{P}_{\nu_\alpha \to \nu_\beta}(E) \phi^{i}_{\alpha}(E) \mathrm{d}E, \quad (5)$$

where we assume a single power-law spectrum for the production flux of astrophysical neutrinos and integrate it. Finally, we calculate the flavour ratio of astrophysical neutrino flavour β on Earth by normalizing it, that is

$$f^{\oplus}_{\beta} = \bar{\phi}^{\oplus}_{\beta} / \sum_\gamma \bar{\phi}^{\oplus}_{\gamma}. \quad (6)$$

In this analysis, a total of 14 systematic error nuisance parameters are simultaneously constrained. The first are the following six oscillation parameters[17]: two neutrino mass-square differences, $\Delta m^2_{21} = 7.42^{+0.21}_{-0.20}\,(\times 10^{-5}\,\mathrm{eV}^2)$, $\Delta m^2_{31} = 2.514^{+0.028}_{-0.027}\,(\times 10^{-3}\,\mathrm{eV}^2)$; three mixing angles, $\sin^2\theta_{12} = 0.304^{+0.013}_{-0.012}$, $\sin^2\theta_{23} = 0.570^{+0.018}_{-0.024}$ and $\sin^2\theta_{31} = 0.02221^{+0.00068}_{-0.00062}$, and the Dirac *CP*-violating phase, δ_{CP} (no constraint). Second are five flux systematics, which can be classified into two categories: the normalization of each flux component, and the spectral index assuming a single power law. The normalization systematic errors are introduced as shifts from the nominal predictions, including astrophysical neutrino flux (Φ_{astro}, no constraint), atmospheric neutrino conventional flux (Φ_{conv}, 40%), prompt flux (Φ_{prompt}, no constraint) and atmospheric muon flux (Φ_{muon}, 50%). The astrophysical neutrino spectral index (γ_{astro}, no constraint) is also included as a systematic error, where this analysis returns a similar best-fit value as in a dedicated study of the same sample[9]. We also introduce three detector systematic parameters: the DOM overall efficiency (ϵ_{DOM}, 10%), DOM angular dependence ($\epsilon_{\mathrm{head\text{-}on}}$, 50%) and the in-ice photon propagation anisotropy around DOMs (a_s, 20%). Additional systematic errors arising from the modelling of atmospheric neutrinos and cosmic rays are used in other analyses[9,10]. These systematics are not considered in this analysis, because they mostly affect low-energy events (<100 TeV). Here, the limit we set for QG-motivated physics depends on the highest end tail of the event distribution.

To place our limits we use two independent analysis methods based on frequentist and Bayesian approaches[35,36]. The Bayesian approach was chosen to be the official result of this analysis because of its accuracy. The faster frequentist approach was used to check the Bayesian results. Both methods use the same 15-dimensional likelihood function with 14 systematic errors, where one parameter represents a new physics scale. In the Bayesian case, the evidence is obtained by marginalizing the same likelihood over the systematic parameters via nested sampling. The marginalization is done assuming model priors from ref. [9]. We use the MultiNest algorithm[37] with 800 live points, ~18,000 steps and a tolerance of 0.05. An example of a posterior distribution from one configuration is shown in Extended Data Fig. 1. Here, the log-likelihood is calculated for $\mathrm{Re}\,(\mathring{c}^{(6)}_{\tau\tau}) = 10^{-44}\,\mathrm{GeV}^{-2}$, with an assumed source flavour ratio $(1{:}0{:}0)_S$. We run nearly ~200,000 similar calculations with different configurations to map out the parameter phase space to find the signal.

We then define the BF to be the ratio of the model evidence with respect to the null hypothesis. We use Jeffreys' scale to set substantial and strong limits that are defined by the BF to be larger than 10 (substantial limit) and 31.6 (strong limit). Extended Data Fig. 2 shows an example of such a plot. Here, multiple sample runs are combined to construct a BF distribution with a function of $\mathrm{Re}\,(\mathring{c}^{(6)}_{\tau\tau})$ with an assumed source flavour ratio of $(1{:}0{:}0)_S$. Due to limited statistics, simulated points have errors, and we use a spline function to extrapolate values between points. Extended Data Table 1 list the substantial and strong limits from this procedure for selected source flavour ratio assumptions. Because of the extrapolation we used, we do not have enough accuracy to set limits and our results are presented with one digit.

We repeat a similar BF function construction with different source flavour ratio assumptions, and we construct the limits with a function of source flavour ratio x (Fig. 3). We use a spline function to extrapolate values between points and smooth the limit lines. We repeat this for different dimension operators, and the results are shown in Extended Data Figs. 3–7. The limits of this analysis go stronger for higher dimensions due to the stronger energy dependence (equation (1)). As the dimension increases, limits from astrophysical neutrino interferometry become stronger than atmospheric neutrino interferometry. On the other hand, for dimension-seven and -eight operators, QG-motivated physics is expected to be smaller than E_P^{-3} and E_P^{-4}. This analysis has no sensitivity to the operators with these sizes. The dimension-three and -four operators are renormalizable and we cannot define QG-motivated physics in the same way. In the frequentist case, the likelihood function is used to find the best-fit point. Then, the profile likelihood ratio of the best fit to the null hypothesis is used to set limits assuming Wilks' theorem. However, Wilks' theorem may not hold in the full likelihood space, which affects the limits obtained. We used distributed Open Science Grid[38] computational resources to perform both analyses.

Data availability

The data events and simulation used in this analysis are described in ref. [9] and files are available from ref. [39].

Code availability

Much of the analysis code is IceCube proprietary and exists as part of the IceCube simulation and production framework. IceCube open-source code can be found at https://github.com/icecube. Additional information is available from analysis@icecube.wisc.edu upon request.

References

34. Argüelles, C. A., Katori, T. & Salvado, J. New physics in astrophysical neutrino flavor. *Phys. Rev. Lett.* **115**, 161303 (2015).
35. Mandalia, S. *Searching for Quantum Gravity with Neutrinos, Optical Module Beam Test at Fermilab and Hadronization Model Studies for IceCube*. PhD thesis, Queen Mary Univ. of London (2020); https://qmro.qmul.ac.uk/xmlui/handle/123456789/69453
36. Farrag, K. *From Infinite to Zero Redshift, Searches for Beyond the Standard Neutrino Model Physics Using Radio Telescopes and Astrophysical Neutrinos in IceCube*. PhD thesis, Queen Mary Univ. of London (2022).
37. Feroz, F., Hobson, M. P. & Bridges, M. MultiNest: an efficient and robust Bayesian inference tool for cosmology and particle physics. *Mon. Not. R. Astron. Soc.* **398**, 1601–1614 (2009).
38. Pordes, R. et al. The Open Science Grid. *J. Phys. Conf. Ser.* **78**, 012057 (2007).
39. IceCube Collaboration. HESE 7.5 year data release (2021); https://doi.org/10.21234/4EQJ-BB17

Acknowledgements

We acknowledge support from the following agencies and institutions: USA—US National Science Foundation–Office of Polar Programs, US National Science Foundation–Physics Division, US National Science Foundation–EPSCoR, Wisconsin Alumni Research Foundation, Center for High Throughput Computing (CHTC) at the University of Wisconsin–Madison, Open Science Grid (OSG), Extreme Science and Engineering Discovery Environment (XSEDE), Frontera computing project at the Texas Advanced Computing Center, US Department of Energy–National Energy Research Scientific Computing Center, Particle Astrophysics Research Computing Center at the University of Maryland, Institute for Cyber-Enabled Research at Michigan State University, and Astroparticle Physics Computational Facility at Marquette University; Belgium—Funds for Scientific Research (FRS-FNRS and FWO), FWO Odysseus and Big Science programmes, and Belgian Federal Science Policy Office (Belspo); Germany—Bundesministerium für Bildung und Forschung (BMBF), Deutsche Forschungsgemeinschaft (DFG), Helmholtz Alliance for Astroparticle Physics (HAP), Initiative and Networking Fund of the Helmholtz Association, Deutsches Elektronen Synchrotron (DESY) and High Performance Computing Cluster of the RWTH Aachen; Sweden—Swedish Research Council, Swedish Polar Research Secretariat, Swedish National Infrastructure for Computing (SNIC) and Knut and Alice Wallenberg Foundation; Australia—Australian Research Council; Canada—Natural Sciences and Engineering Research Council of Canada, Calcul Québec, Compute Ontario, Canada Foundation for Innovation, WestGrid and Compute Canada; Denmark—Villum Fonden and Carlsberg Foundation; New Zealand—Marsden Fund; Japan—Japan Society for Promotion of Science (JSPS) and Institute for Global Prominent Research (IGPR) of Chiba University; Korea—National Research Foundation of Korea (NRF); Switzerland—Swiss National Science Foundation (SNSF); United Kingdom—Department of Physics, University of Oxford, the Royal Society and the Science and Technology Facilities Council (STFC).

Author contributions

The IceCube Collaboration acknowledges the significant contributions to this manuscript from C. Argüelles, K. Farrag and T. Katori. The IceCube Collaboration designed, constructed and now operates the IceCube Neutrino Observatory. Data processing and calibration, Monte Carlo simulations of the detector and of theoretical models, and data analyses were performed by a large number of collaboration members, who also discussed and approved the scientific results presented here.

Competing interests

The authors declare no competing interests.

Additional information

Extended data is available for this paper at https://doi.org/10.1038/s41567-022-01762-1.

Peer review information *Nature Physics* thanks Giulia Gubitosi, Sergio Navas and the other, anonymous, reviewer(s) for their contribution to the peer review of this work.

Reprints and permissions information is available at www.nature.com/reprints.

 https://doi.org/10.1038/s41567-022-01762-1

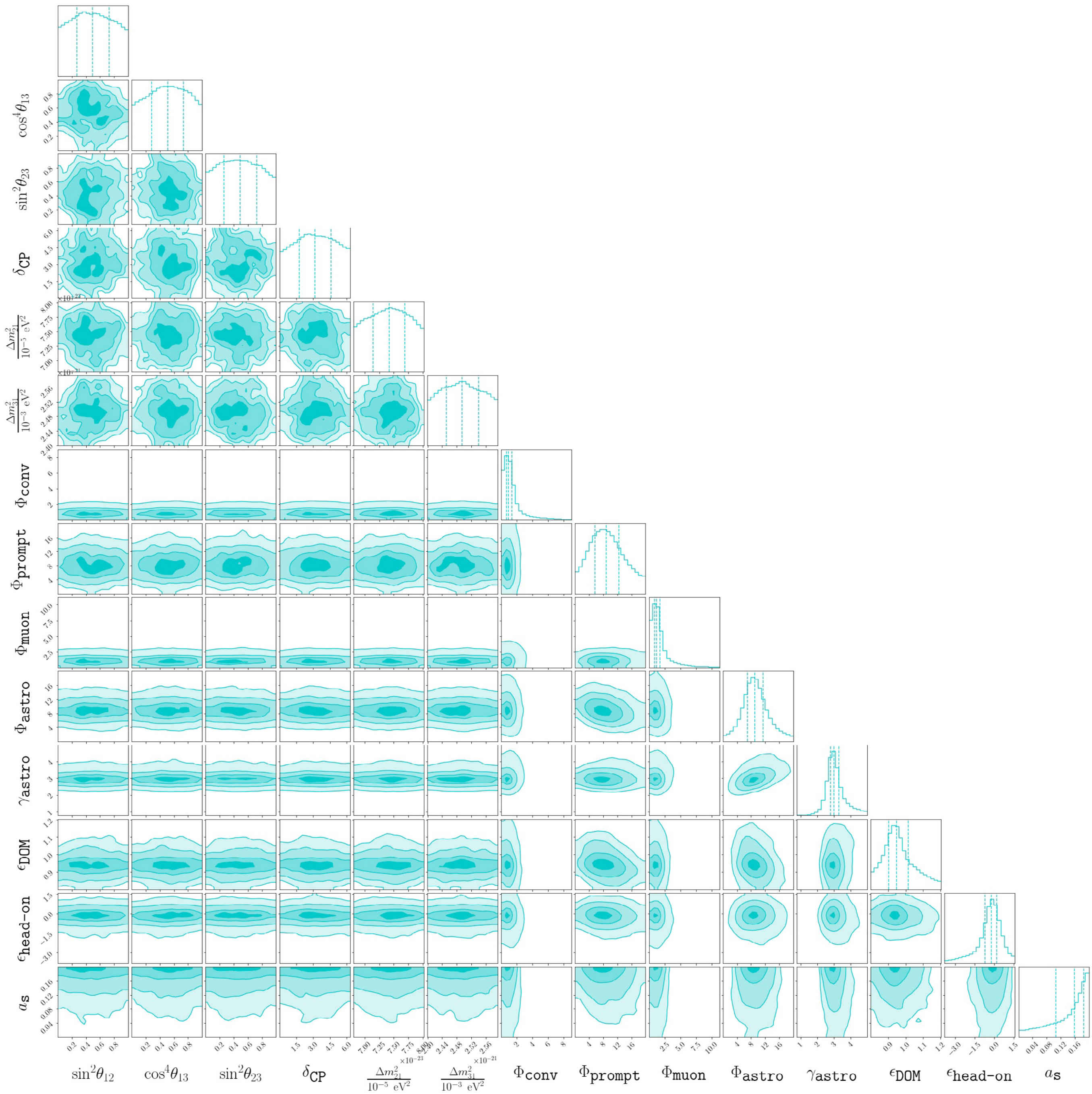

Extended Data Fig. 1 | Example posterior distribution over the 14 nuisance parameters. The plot is for $\mathrm{Re}(\mathring{c}^{(6)}_{\tau\tau}) = 10^{-44}\ GeV^{-2}$ with source combination $(0{:}\,1{:}\,0)_S$. Blue contours show two dimensional distribution slices, with one-dimensional projections above for each parameter. Three vertical lines indicate the lower quartile (25%), median (50%) and upper quartile (75%) for each parameter. Parameters are introduced in Ref. [9].

https://doi.org/10.1038/s41567-022-01762-1

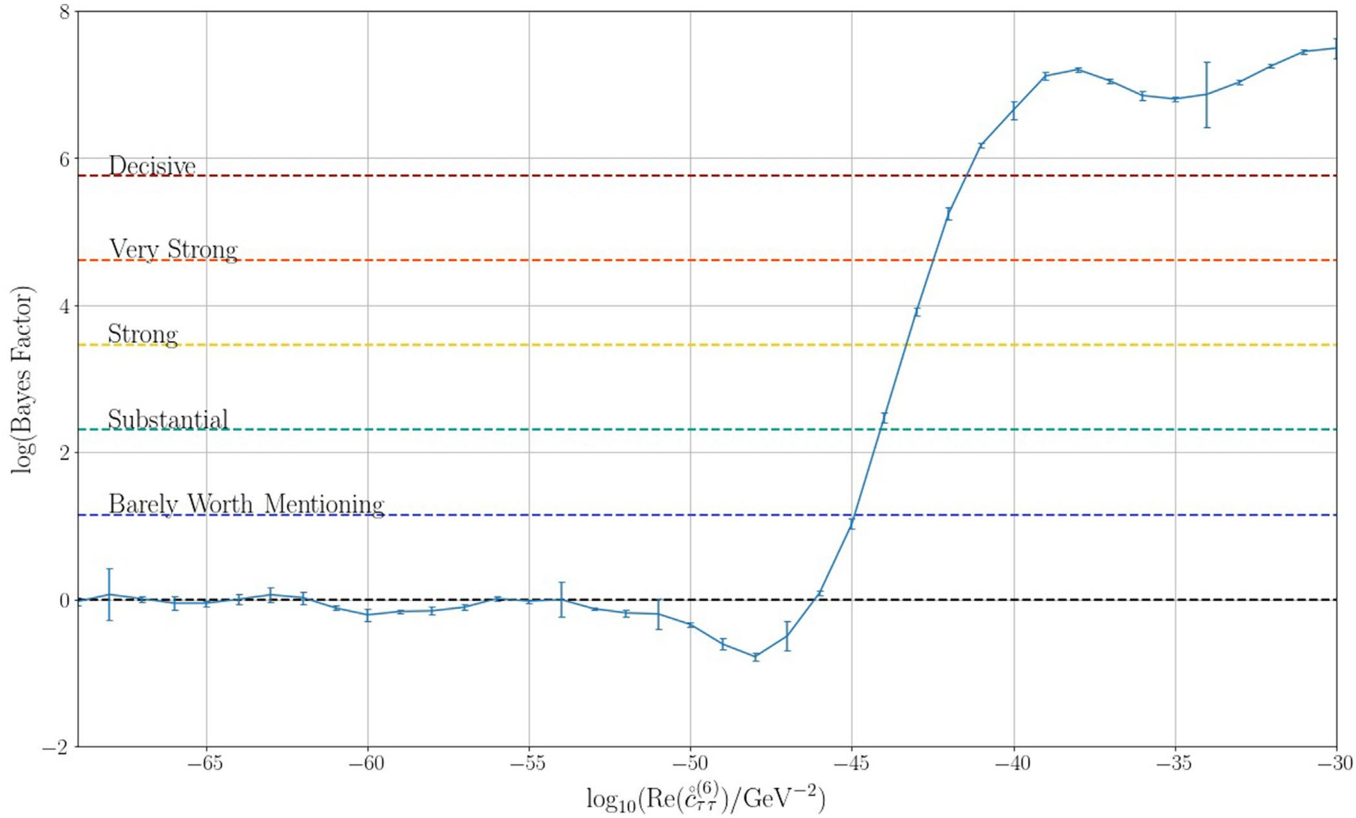

Extended Data Fig. 2 | Example of the analysis Bayes factor as a function of one of the constrained parameters. Horizontal lines show different hypothesis rejection strength levels according to Jeffreys' scale. Here, we set the limit on $\mathrm{Re}(\mathring{c}^{(6)}_{\tau\tau})$ with an assumed source flavour ratio $(0:1:0)_S$. A substantial limit is obtained when the Bayes factor is greater than 10.0, and strong limits when the Bayes factor is greater than 31.6. Error bars indicate the error on the evidence computation via nested sampling.

https://doi.org/10.1038/s41567-022-01762-1

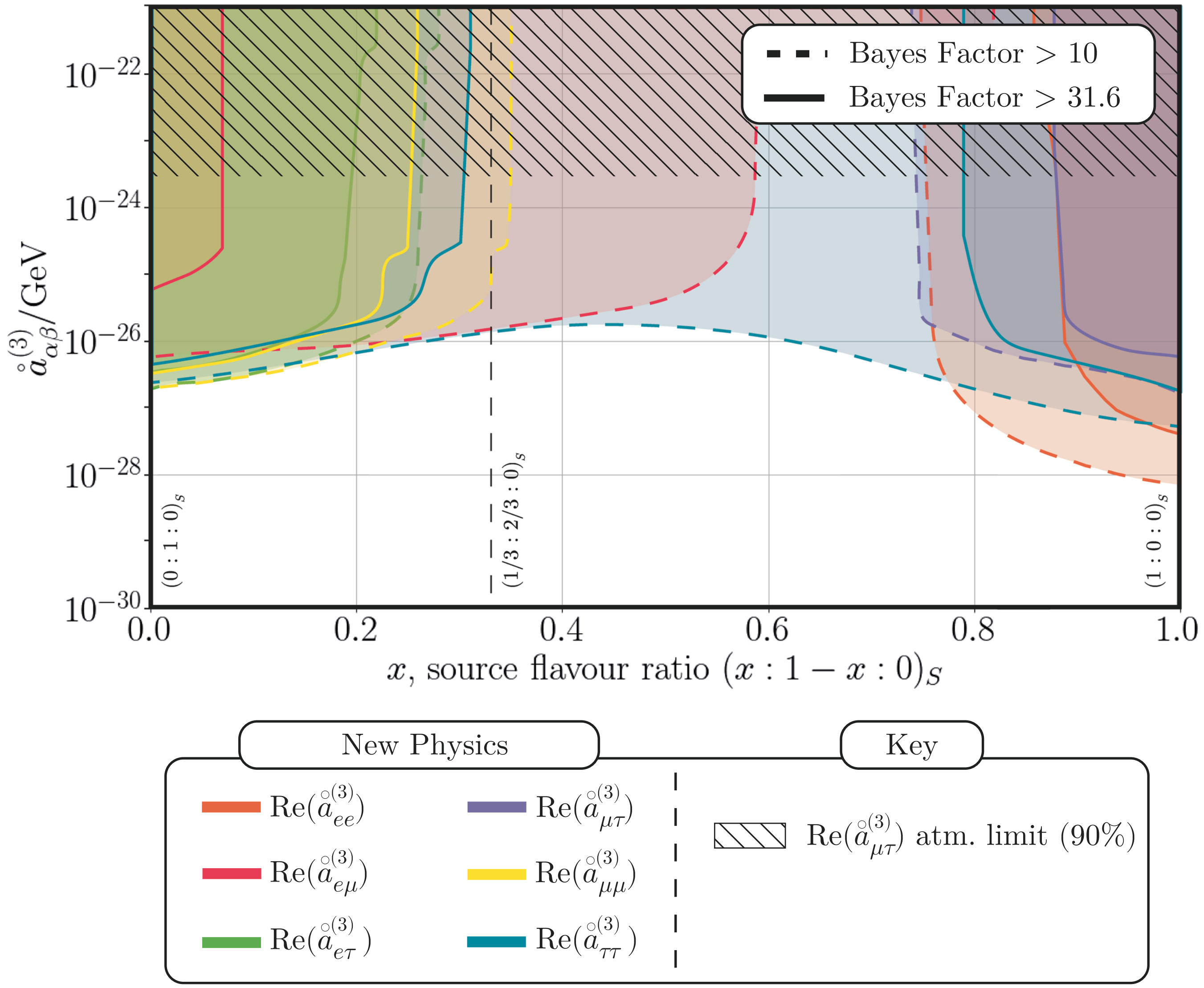

Extended Data Fig. 3 | Limits on the dimension-three new physics operator. The hatched region is the limit obtained from the atmospheric neutrino data analysis on $\mathrm{Re}(\mathring{a}^{(3)}_{\mu\tau})$[15]. Limits determined by Bayes factors > 10 (dashed lines) and > 31.6 (solid lines) are presented as a function of the assumed astrophysical neutrino flavour ratio at the production source. The leftmost scenario is ν_μ dominant $(0{:}1{:}0)_S$ and the rightmost is ν_e dominant $(1{:}0{:}0)_S$. The preferred scenario corresponds to $(1/3{:}2/3{:}0)_S$ (dashed vertical line). Limits on $\mathrm{Re}(\mathring{a}^{(3)}_{ee})$ on (orange), $\mathrm{Re}(\mathring{a}^{(3)}_{e\mu})$ (red), $\mathrm{Re}(\mathring{a}^{(3)}_{e\tau})$ (green), $\mathrm{Re}(\mathring{a}^{(3)}_{\mu\mu})$ (yellow), $\mathrm{Re}(\mathring{a}^{(3)}_{\mu\tau})$ (purple), and $\mathrm{Re}(\mathring{a}^{(3)}_{\tau\tau})$ (blue) are shown.

https://doi.org/10.1038/s41567-022-01762-1

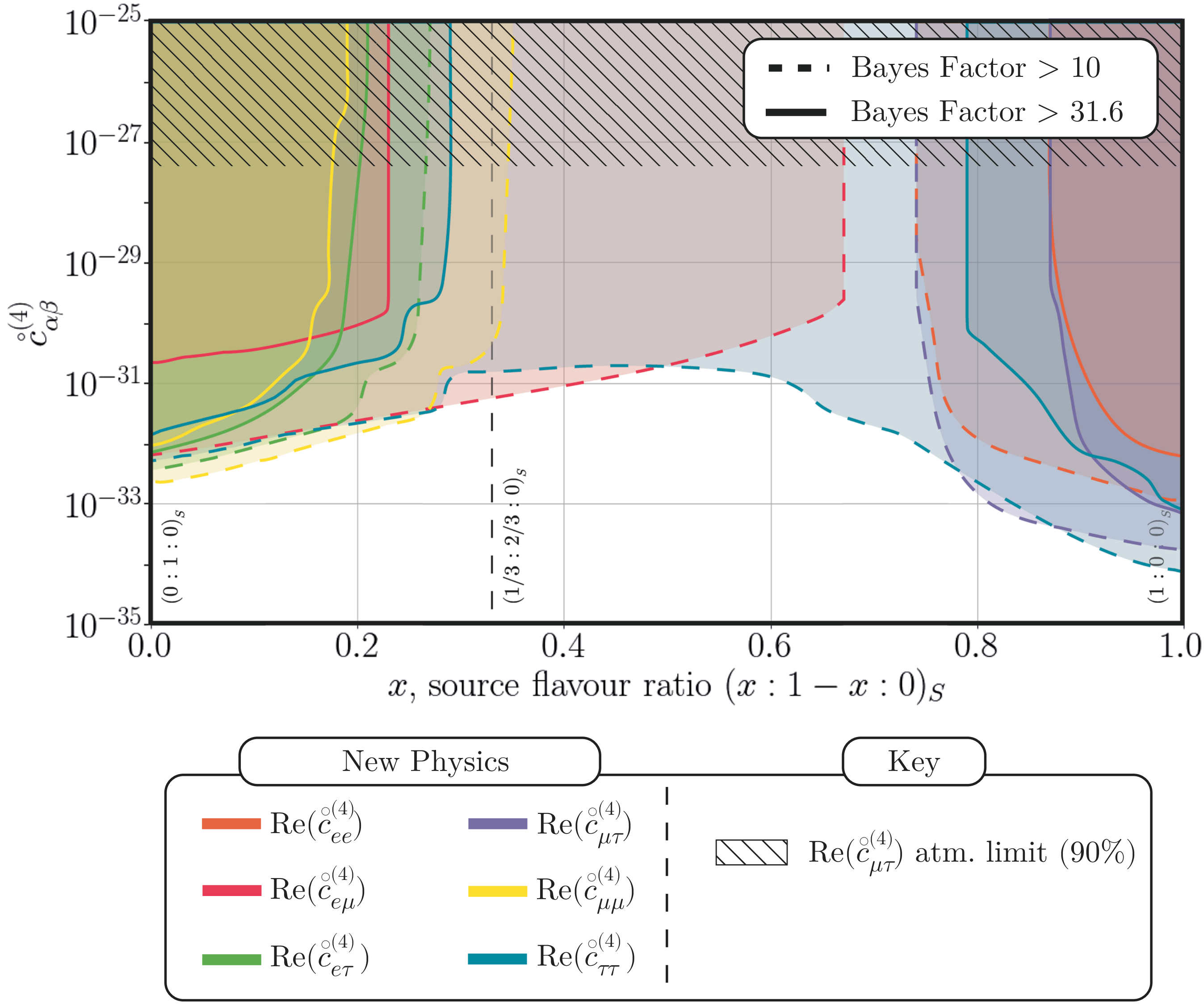

Extended Data Fig. 4 | Limits on the dimension-four new physics operator. The hatched region is the limit obtained from the atmospheric neutrino data analysis on $\mathrm{Re}(\mathring{c}^{(4)}_{\mu\tau})$[15]. Limits determined by Bayes factors > 10 (dashed lines) and > 31.6 (solid lines) are presented as a function of the assumed astrophysical neutrino flavour ratio at the production source. The leftmost scenario is ν_μ dominant $(0: 1: 0)_S$ and the rightmost is ν_e dominant $(1: 0: 0)_S$. The preferred scenario corresponds to $(1/3: 2/3: 0)_S$ (dashed vertical line). Limits on $\mathrm{Re}(\mathring{c}^{(4)}_{ee})$ on (orange), $\mathrm{Re}(\mathring{c}^{(4)}_{e\mu})$ (red), $\mathrm{Re}(\mathring{c}^{(4)}_{e\tau})$ (green), $\mathrm{Re}(\mathring{c}^{(4)}_{\mu\mu})$ (yellow), $\mathrm{Re}(\mathring{c}^{(4)}_{\mu\tau})$ (purple), and $\mathrm{Re}(\mathring{c}^{(4)}_{\tau\tau})$ (blue) are shown.

 https://doi.org/10.1038/s41567-022-01762-1

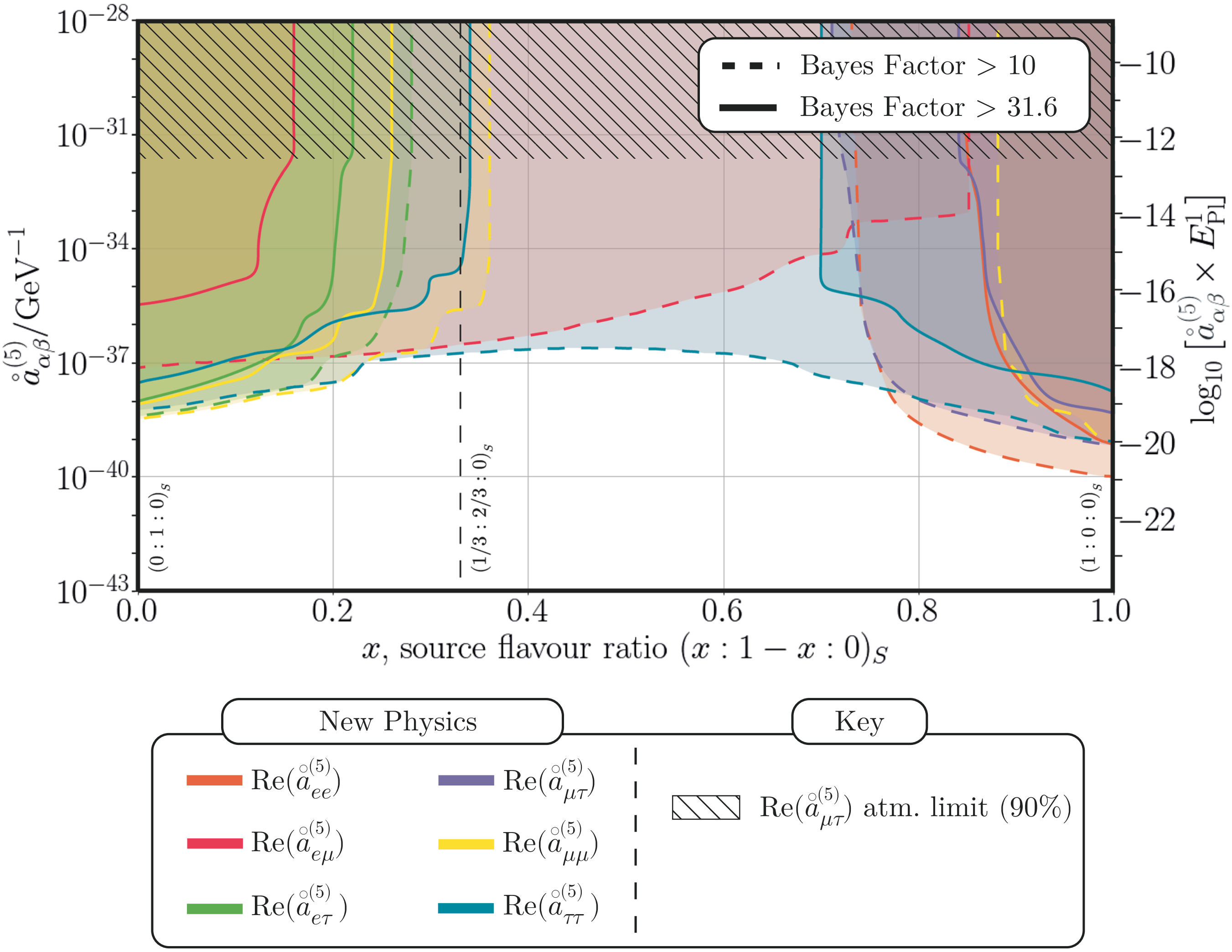

Extended Data Fig. 5 | Limits on the dimension-five new physics operator. The hatched region is the limit obtained from the atmospheric neutrino data analysis on $\mathrm{Re}(\mathring{a}^{(5)}_{\mu\tau})$[15]. Limits determined by Bayes factors > 10 (dashed lines) and > 31.6 (solid lines) are presented as a function of the assumed astrophysical neutrino flavour ratio at the production source. The leftmost scenario is ν_μ dominant $(0:1:0)_S$ and the rightmost is ν_e dominant $(1:0:0)_S$. The preferred scenario corresponds to $(1/3:2/3:0)_S$ (dashed vertical line). Limits on $\mathrm{Re}(\mathring{a}^{(5)}_{ee})$ on (orange), $\mathrm{Re}(\mathring{a}^{(5)}_{e\mu})$ (red), $\mathrm{Re}(\mathring{a}^{(5)}_{e\tau})$ (green), $\mathrm{Re}(\mathring{a}^{(5)}_{\mu\mu})$ (yellow), $\mathrm{Re}(\mathring{a}^{(5)}_{\mu\tau})$ (purple), and $\mathrm{Re}(\mathring{a}^{(5)}_{\tau\tau})$ (blue) are shown.

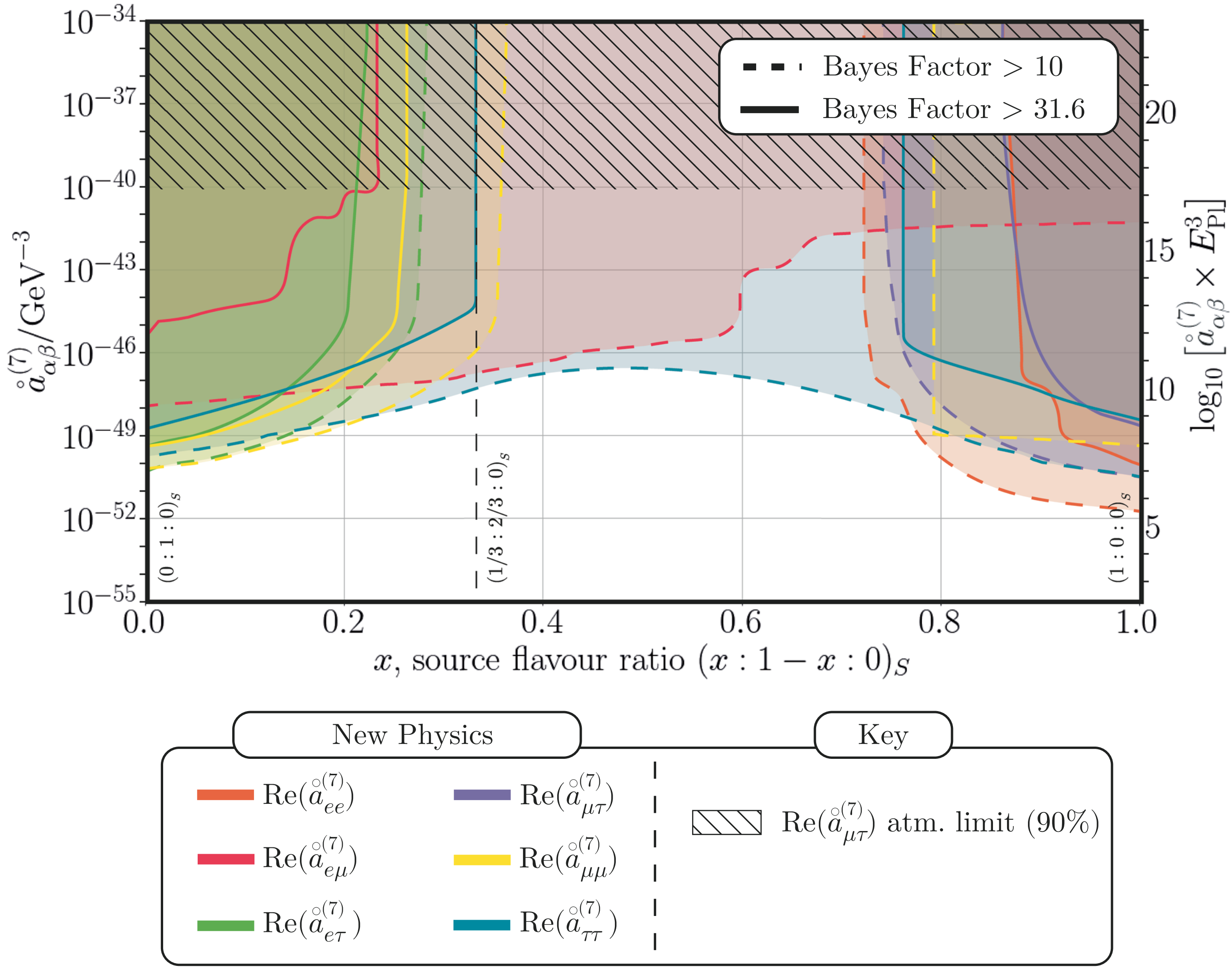

Extended Data Fig. 6 | Limits on the dimension-seven new physics operator. The hatched region is the limit obtained from the atmospheric neutrino data analysis on Re($\mathring{a}^{(7)}_{\mu\tau}$)[15]. Limits determined by Bayes factors > 10 (dashed lines) and > 31.6 (solid lines) are presented as a function of the assumed astrophysical neutrino flavour ratio at the production source. The leftmost scenario is ν_μ dominant $(0:1:0)_S$ and the rightmost is ν_e dominant $(1:0:0)_S$. The preferred scenario corresponds to $(1/3:2/3:0)_S$ (dashed vertical line). Limits on Re($\mathring{a}^{(7)}_{ee}$) on (orange), Re($\mathring{a}^{(7)}_{e\mu}$) (red), Re($\mathring{a}^{(7)}_{e\tau}$) (green), Re($\mathring{a}^{(7)}_{\mu\mu}$) (yellow), Re($\mathring{a}^{(7)}_{\mu\tau}$) (purple), and Re($\mathring{a}^{(7)}_{\tau\tau}$) (blue) are shown.

 https://doi.org/10.1038/s41567-022-01762-1

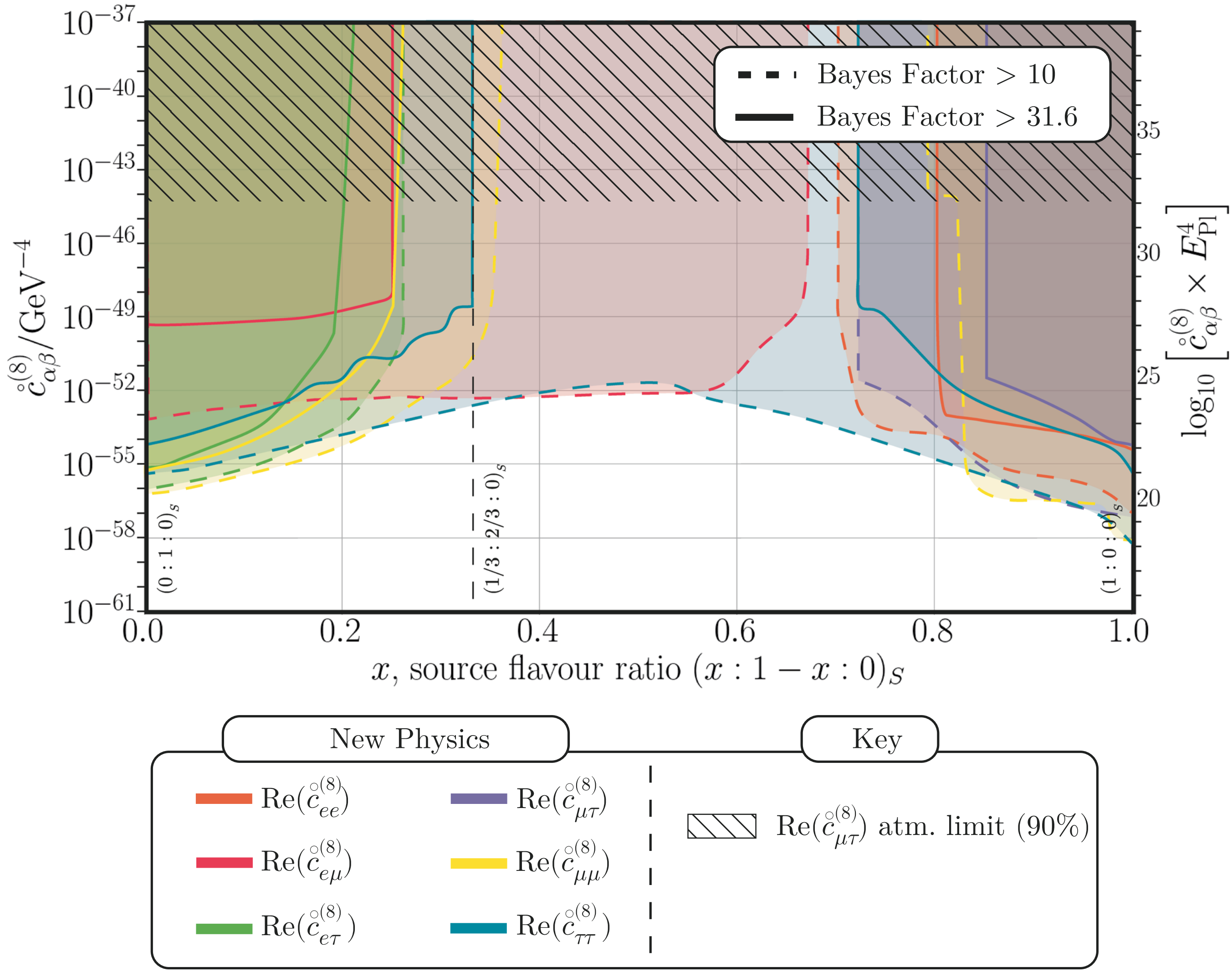

Extended Data Fig. 7 | Limits on the dimension-eight new physics operator. The hatched region is the limit obtained from the atmospheric neutrino data analysis on [15]. Limits determined by Bayes factors > 10 (dashed lines) and > 31.6 (solid lines) are presented as a function of the assumed astrophysical neutrino flavour ratio at the production source. The leftmost scenario is ν_μ dominant $(0:1:0)_S$ and the rightmost is ν_e dominant $(1:0:0)_S$. The preferred scenario corresponds to $(1/3:2/3:0)_S$ (dashed vertical line). Limits on Re($\mathring{c}^{(8)}_{ee}$) on (orange), Re($\mathring{c}^{(8)}_{e\mu}$) (red), Re($\mathring{c}^{(8)}_{e\tau}$) (green), Re($\mathring{c}^{(8)}_{\mu\mu}$) (yellow), Re($\mathring{c}^{(8)}_{\mu\tau}$) (purple), and Re($\mathring{c}^{(8)}_{\tau\tau}$) (blue) are shown.

 https://doi.org/10.1038/s41567-022-01762-1

dim	coefficient	limit (Bayes Factor> 10.0)	limit (Bayes Factor> 31.6)	dim	coefficient	limit (Bayes Factor> 10.0)	limit (Bayes Factor> 31.6)	$(f_e : f_\mu : f_\tau)_S$
3	$\mathrm{Re}\,(\mathring{a}^{(3)}_{e\mu})$	6×10^{-27} GeV	6×10^{-26} GeV	4	$\mathrm{Re}\,(\mathring{c}^{(4)}_{e\mu})$	6×10^{-33}	2×10^{-31}	$(0:1:0)_S$
	$\mathrm{Re}\,(\mathring{a}^{(3)}_{e\tau})$	2×10^{-27} GeV	3×10^{-27} GeV		$\mathrm{Re}\,(\mathring{c}^{(4)}_{e\tau})$	4×10^{-33}	7×10^{-33}	$(0:1:0)_S$
	$\mathrm{Re}\,(\mathring{a}^{(3)}_{\mu\mu})$	2×10^{-27} GeV	3×10^{-27} GeV		$\mathrm{Re}\,(\mathring{c}^{(4)}_{\mu\mu})$	2×10^{-33}	5×10^{-33}	$(0:1:0)_S$
	$\mathrm{Re}\,(\mathring{a}^{(3)}_{\tau\tau})$	2×10^{-27} GeV	5×10^{-27} GeV		$\mathrm{Re}\,(\mathring{c}^{(4)}_{\tau\tau})$	5×10^{-33}	1×10^{-32}	$(0:1:0)_S$
	$\mathrm{Re}\,(\mathring{a}^{(3)}_{e\mu})$	1×10^{-26} GeV	—		$\mathrm{Re}\,(\mathring{c}^{(4)}_{e\mu})$	5×10^{-32}	—	$(1/3:2/3:0)_S$
	$\mathrm{Re}\,(\mathring{a}^{(3)}_{\mu\mu})$	2×10^{-25} GeV	—		$\mathrm{Re}\,(\mathring{c}^{(4)}_{\mu\mu})$	5×10^{-31}	—	$(1/3:2/3:0)_S$
	$\mathrm{Re}\,(\mathring{a}^{(3)}_{\tau\tau})$	1×10^{-26} GeV	—		$\mathrm{Re}\,(\mathring{c}^{(4)}_{\tau\tau})$	1×10^{-31}	—	$(1/3:2/3:0)_S$
	$\mathrm{Re}\,(\mathring{a}^{(3)}_{ee})$	7×10^{-29} GeV	4×10^{-28} GeV		$\mathrm{Re}\,(\mathring{c}^{(4)}_{ee})$	9×10^{-34}	6×10^{-33}	$(1:0:0)_S$
	$\mathrm{Re}\,(\mathring{a}^{(3)}_{\mu\tau})$	3×10^{-27} GeV	6×10^{-27} GeV		$\mathrm{Re}\,(\mathring{c}^{(4)}_{\mu\tau})$	2×10^{-34}	7×10^{-34}	$(1:0:0)_S$
	$\mathrm{Re}\,(\mathring{a}^{(3)}_{\tau\tau})$	5×10^{-28} GeV	2×10^{-27} GeV		$\mathrm{Re}\,(\mathring{c}^{(4)}_{\tau\tau})$	7×10^{-35}	8×10^{-34}	$(1:0:0)_S$
5	$\mathrm{Re}\,(\mathring{a}^{(5)}_{e\mu})$	7×10^{-38} GeV^{-1}	3×10^{-36} GeV^{-1}	6	$\mathrm{Re}\,(\mathring{c}^{(6)}_{e\mu})$	3×10^{-43} GeV^{-2}	4×10^{-41} GeV^{-2}	$(0:1:0)_S$
	$\mathrm{Re}\,(\mathring{a}^{(5)}_{e\tau})$	4×10^{-39} GeV^{-1}	9×10^{-39} GeV^{-1}		$\mathrm{Re}\,(\mathring{c}^{(6)}_{e\tau})$	6×10^{-45} GeV^{-2}	3×10^{-44} GeV^{-2}	$(0:1:0)_S$
	$\mathrm{Re}\,(\mathring{a}^{(5)}_{\mu\mu})$	3×10^{-39} GeV^{-1}	8×10^{-39} GeV^{-1}		$\mathrm{Re}\,(\mathring{c}^{(6)}_{\mu\mu})$	2×10^{-45} GeV^{-2}	7×10^{-45} GeV^{-2}	$(0:1:0)_S$
	$\mathrm{Re}\,(\mathring{a}^{(5)}_{\tau\tau})$	6×10^{-39} GeV^{-1}	3×10^{-38} GeV^{-1}		$\mathrm{Re}\,(\mathring{c}^{(6)}_{\tau\tau})$	8×10^{-45} GeV^{-2}	1×10^{-43} GeV^{-2}	$(0:1:0)_S$
	$\mathrm{Re}\,(\mathring{a}^{(5)}_{e\mu})$	2×10^{-37} GeV^{-1}	—		$\mathrm{Re}\,(\mathring{c}^{(6)}_{e\mu})$	8×10^{-43} GeV^{-2}	—	$(1/3:2/3:0)_S$
	$\mathrm{Re}\,(\mathring{a}^{(5)}_{\mu\mu})$	2×10^{-36} GeV^{-1}	—		$\mathrm{Re}\,(\mathring{c}^{(6)}_{\mu\mu})$	2×10^{-42} GeV^{-2}	—	$(1/3:2/3:0)_S$
	$\mathrm{Re}\,(\mathring{a}^{(5)}_{\tau\tau})$	2×10^{-37} GeV^{-1}	—		$\mathrm{Re}\,(\mathring{c}^{(6)}_{\tau\tau})$	1×10^{-42} GeV^{-2}	—	$(1/3:2/3:0)_S$
	$\mathrm{Re}\,(\mathring{a}^{(5)}_{ee})$	9×10^{-41} GeV^{-1}	7×10^{-40} GeV^{-1}		$\mathrm{Re}\,(\mathring{c}^{(6)}_{ee})$	1×10^{-45} GeV^{-2}	2×10^{-44} GeV^{-2}	$(1:0:0)_S$
	$\mathrm{Re}\,(\mathring{a}^{(5)}_{\mu\mu})$	8×10^{-40} GeV^{-1}	—		$\mathrm{Re}\,(\mathring{c}^{(6)}_{\mu\mu})$	4×10^{-46} GeV^{-2}	—	$(1:0:0)_S$
	$\mathrm{Re}\,(\mathring{a}^{(5)}_{\mu\tau})$	6×10^{-40} GeV^{-1}	4×10^{-39} GeV^{-1}		$\mathrm{Re}\,(\mathring{c}^{(6)}_{\mu\tau})$	3×10^{-46} GeV^{-2}	6×10^{-45} GeV^{-2}	$(1:0:0)_S$
	$\mathrm{Re}\,(\mathring{a}^{(5)}_{\tau\tau})$	8×10^{-40} GeV^{-1}	2×10^{-38} GeV^{-1}		$\mathrm{Re}\,(\mathring{c}^{(6)}_{\tau\tau})$	1×10^{-46} GeV^{-2}	6×10^{-45} GeV^{-2}	$(1:0:0)_S$
7	$\mathrm{Re}\,(\mathring{a}^{(7)}_{e\mu})$	1×10^{-48} GeV^{-3}	5×10^{-46} GeV^{-3}	8	$\mathrm{Re}\,(\mathring{c}^{(8)}_{e\mu})$	7×10^{-54} GeV^{-4}	1×10^{-50} GeV^{-4}	$(0:1:0)_S$
	$\mathrm{Re}\,(\mathring{a}^{(7)}_{e\tau})$	5×10^{-51} GeV^{-3}	4×10^{-50} GeV^{-3}		$\mathrm{Re}\,(\mathring{c}^{(8)}_{e\tau})$	8×10^{-57} GeV^{-4}	6×10^{-56} GeV^{-4}	$(0:1:0)_S$
	$\mathrm{Re}\,(\mathring{a}^{(7)}_{\mu\mu})$	5×10^{-51} GeV^{-3}	4×10^{-50} GeV^{-3}		$\mathrm{Re}\,(\mathring{c}^{(8)}_{\mu\mu})$	6×10^{-57} GeV^{-4}	5×10^{-56} GeV^{-4}	$(0:1:0)_S$
	$\mathrm{Re}\,(\mathring{a}^{(7)}_{\tau\tau})$	2×10^{-50} GeV^{-3}	2×10^{-49} GeV^{-3}		$\mathrm{Re}\,(\mathring{c}^{(8)}_{\tau\tau})$	4×10^{-56} GeV^{-4}	6×10^{-55} GeV^{-4}	$(0:1:0)_S$
	$\mathrm{Re}\,(\mathring{a}^{(7)}_{e\mu})$	2×10^{-47} GeV^{-3}	—		$\mathrm{Re}\,(\mathring{c}^{(8)}_{e\mu})$	5×10^{-53} GeV^{-4}	—	$(1/3:2/3:0)_S$
	$\mathrm{Re}\,(\mathring{a}^{(7)}_{\mu\mu})$	2×10^{-46} GeV^{-3}	—		$\mathrm{Re}\,(\mathring{c}^{(8)}_{\mu\mu})$	2×10^{-51} GeV^{-4}	—	$(1/3:2/3:0)_S$
	$\mathrm{Re}\,(\mathring{a}^{(7)}_{\tau\tau})$	3×10^{-48} GeV^{-3}	3×10^{-45} GeV^{-3}		$\mathrm{Re}\,(\mathring{c}^{(8)}_{\tau\tau})$	2×10^{-53} GeV^{-4}	—	$(1/3:2/3:0)_S$
	$\mathrm{Re}\,(\mathring{a}^{(7)}_{ee})$	1×10^{-52} GeV^{-3}	8×10^{-51} GeV^{-3}		$\mathrm{Re}\,(\mathring{c}^{(8)}_{ee})$	1×10^{-57} GeV^{-4}	3×10^{-55} GeV^{-4}	$(1:0:0)_S$
	$\mathrm{Re}\,(\mathring{a}^{(7)}_{e\mu})$	6×10^{-42} GeV^{-3}	—		$\mathrm{Re}\,(\mathring{c}^{(8)}_{e\mu})$	—	—	$(1:0:0)_S$
	$\mathrm{Re}\,(\mathring{a}^{(7)}_{\mu\mu})$	4×10^{-50} GeV^{-3}	—		$\mathrm{Re}\,(\mathring{c}^{(8)}_{\mu\mu})$	6×10^{-59} GeV^{-4}	—	$(1:0:0)_S$
	$\mathrm{Re}\,(\mathring{a}^{(7)}_{\mu\tau})$	3×10^{-51} GeV^{-3}	2×10^{-49} GeV^{-3}		$\mathrm{Re}\,(\mathring{c}^{(8)}_{\mu\tau})$	6×10^{-58} GeV^{-4}	5×10^{-55} GeV^{-4}	$(1:0:0)_S$
	$\mathrm{Re}\,(\mathring{a}^{(7)}_{\tau\tau})$	3×10^{-51} GeV^{-3}	3×10^{-49} GeV^{-3}		$\mathrm{Re}\,(\mathring{c}^{(8)}_{\tau\tau})$	5×10^{-59} GeV^{-4}	8×10^{-56} GeV^{-4}	$(1:0:0)_S$

Extended Data Table 1 | Limits on new physics operators extracted from this analysis. These limits on new physics operators are derived from Bayes factor > 10.0 (Bayes factor > 31.6) which corresponds to 1 in 10.0 (31.6) likelihood ratio for a uniform prior. They are for characteristic source flavour ratios, $(1{:}\,0{:}\,0)_S$, $(1/3{:}\,2/3{:}\,0)_S$, and $(0{:}\,1{:}\,0)_S$. We list only operators where limits are set.